Japanese Journal of Applied Physics

The Japan Society of Applied Physics

REGULAR PAPER

Design guides for artificial photosynthetic devices consisting of voltage-matched perovskite/silicon tandem solar-cell modules and electrochemical reactor modules

To cite this article: Yasuhiko Takeda *et al* 2023 *Jpn. J. Appl. Phys.* **62** SK1018

Japanese Journal of Applied Physics **62**, SK1018 (2023)
https://doi.org/10.35848/1347-4065/acc3a5

REGULAR PAPER

Design guides for artificial photosynthetic devices consisting of voltage-matched perovskite/silicon tandem solar-cell modules and electrochemical reactor modules

Yasuhiko Takeda*, Ken-ichi Yamanaka, Takeshi Morikawa, and Naohiko Kato

Toyota Central Research and Development Laboratories, Inc., Nagakute, Aichi 480-1192, Japan

*E-mail: takeda@mosk.tytlabs.co.jp

Received December 20, 2022; revised February 14, 2023; accepted March 12, 2023; published online April 20, 2023

We clarified the design guides for H_2- and CO-producing artificial photosynthetic devices. The combination of a voltage-matched (VM) tandem solar-cell (SC) module and an electrochemical (EC) module was adopted. The parallel-connected top and bottom SC modules, in which multiple organic–inorganic hybrid perovskite (PVK) SCs with a bandgap of 1.7 eV and crystalline-silicon SCs were connected in series, respectively, powered the EC module consisting of series-connected multiple EC reactors. It was found that the design parameters of the series connection numbers must be optimized under slightly greater solar intensity and higher temperature than the average values to minimize the mismatch between the device operating voltage and SC maximal power voltage. This is in contrast to that the annual electricity production of the VM SC module coupled with a power conditioner is not sensitive to the optimization conditions. Increases in the bandgaps of the PVK SCs do not affect the annual production significantly.

1. Introduction

Efficient utilization of solar energy is obviously important for carbon neutrality. However, solar photovoltaic power generation currently only accounts for a small part of total electricity production, although crystalline silicon solar cells (Si SCs) are widespread. Therefore, improvements in the solar-to-electricity energy conversion efficiency (η_{SC}) of SCs are strongly desired.[1] In addition, artificial photosynthesis that converts H_2O to H_2 and CO_2 to CO, HCOOH (formic acid), etc. is another means to utilize and store solar energy, as well as to produce alternative fuels and reduce net CO_2 emissions. Therefore, artificial photosynthetic devices consisting of SCs and electrochemical (EC) reactors, which are of the topic of the present study, have been extensively studied.[2–4]

We have tackled the problem to achieve both high efficiency and a practically large size for artificial photosynthetic devices, designing a device consisting of a Si SC module and an EC reactor equipped with 1 m^2-sized electrode catalysts to produce formate, and realized a high solar-to-chemical energy conversion efficiency (η_{STC}) of 10.5%.[5,6] Furthermore, an improvement in the durability of the catalysts[7] and direct conversion of dilute CO_2 in a flue gas[8] are proceeding. On the other hand, an improvement in the η_{SC} of the SCs used in the device will directly lead to a higher η_{STC}, in addition to the development of more active electrode catalysts.

The steadiest way for an improvement in η_{SC} is a tandem configuration,[9,10] in which two or more materials with different bandgaps (E_g) share the light-absorption function. This reduces the energy dissipation caused by carrier thermalization because the light-absorption spectrum of each material narrows. Tandem SCs using group III-V compound semiconductors have been developed and commercialized for concentration photovoltaics and space use.[11] However, the high cost of these group III-V tandem SCs is an obstacle to non-concentration applications and consumer use.

On the other hand, the development of organic–inorganic hybrid perovskite (PVK) SCs has advanced significantly, resulting in high η_{SC} values close to those of Si SCs, as well as improvements in the durability.[12–14] The tunability of E_g by their compositions is one of the great advantages of PVK SCs in addition to potentially low costs. High photovoltaic performance has been realized in an E_g range of 1.2–1.7 eV,[15,16] although an E_g of around 1.5 eV has achieved the highest η_{SC}.[17,18] As shown later (see Fig. 13), $E_g = 1.7$ eV is close to the optimal value for tandem SCs combined with Si SCs. Therefore, tandem PVK/Si SCs[19–21] and their application to artificial photosynthetic devices[22–24] has been studied for the purpose of both high η_{STC} and low cost. The next target should be triple-tandem SCs using two PVKs with different E_g values.[25–27] However, higher η_{SC} or η_{STC} than those for the double-tandem SCs has not yet been realized, because the performance of the PVK SCs at $E_g > 1.7$ eV is not sufficiently high. Therefore, in the present study, we seek the means to improve η_{SC} and η_{STC} using the double-tandem PVK ($E_g = 1.7$ eV)/Si configurations.

We have previously revealed that the voltage-matched (VM) tandem SC modules consisting of parallel-connected PVK top modules and Si bottom modules, in which multiple PVK and Si SCs are connected in series, respectively, yield high η_{SC}.[28] In addition, artificial photosynthetic devices using EC modules, which consist of multiple series-connected EC reactors, powered by VM tandem SC modules yield a higher η_{STC}. Thus, the objective of the present study is to clarify the design guides for artificial photosynthetic devices consisting of VM SC modules and EC modules to achieve higher η_{STC} throughout the year, by investigating the impacts of the solar intensity and SC temperature in detail. In particular, the differences in the effects of these external operating conditions on the performance of the SCs and the SC-EC combinations are elucidated.

2. Basic design of VM tandem SC modules and artificial synthetic devices using these SC modules

Figure 1 illustrates two kinds of PVK/Si tandem SC modules and artificial synthetic devices using these SC modules. When an SC module is coupled with a power conditioner, η_{SC} is the ratio of the maximal value of the output power density that is equal to the product of the current density and voltage to the solar intensity. The two-terminal (2T) SC module using the PVK/Si double-junction SCs displayed in Fig. 1(a) requires current matching between the PVK and Si SCs for a high η_{SC}. This determines the optimal E_g of the PVK SC. However, the current matching breaks when the

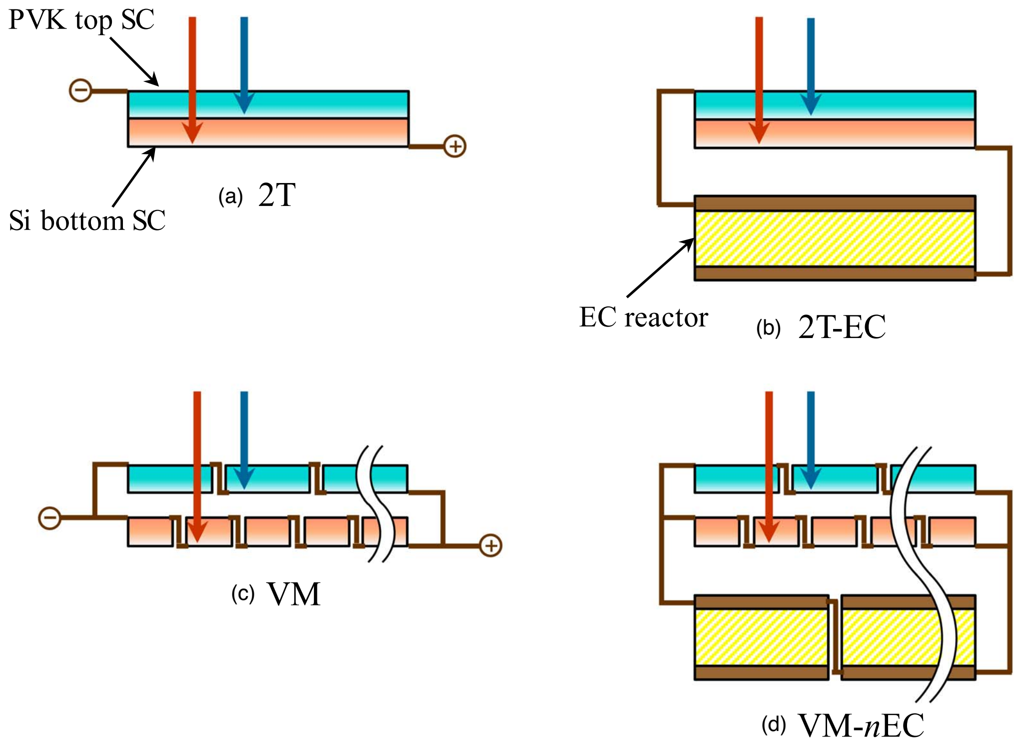

Fig. 1. (a) and (c) Organic–inorganic hybrid PVK/Si tandem SC modules. (b) and (d) Artificial photosynthetic devices consisting of the SC modules and EC modules.

solar spectrum changes, even though it holds for the spectrum used for E_g-optimization. Hence, the 2T SC module suffers from solar spectrum variation.

The intersection of the current density−voltage (J–V) curve of the SC module and the load curve of the EC module determines the operating point (current density J_{op} and voltage V_{op}) of the artificial photosynthetic device. Because the reaction rate increases in proportion to J_{op}, η_{STC} is proportional to J_{op} at a given solar intensity. Therefore, the requisite for a high η_{STC} is that J at $V = V_{op}$ is maximized. This, in turn, requires that the voltage at the maximal power point (V_{MPP}) of the SC module is close to V_{op}. The load curves of the H_2- and CO-producing EC reactors start to increase from 1.4–1.6 V which are higher than the thermodynamic threshold voltages (1.23 V for H_2 production from H_2O, and 1.34 V for CO production from CO_2) by the overvoltages required for promoting the reactions. Therefore, V_{op} is slightly higher than 1.4–1.6 V (1.5–1.7 V in reality; see Figs. 9 and 12). However, the E_g of the PVK SC used in the 2T SC module is determined from the current matching condition, as stated above. Hence, V_{op} of the artificial photosynthetic 2T-EC device using the 2T SC module shown in Fig. 1(b) does not coincide with V_{MPP} of the SC module in general, resulting in a low η_{STC}.

The VM tandem SC module illustrated in Fig. 1(c) solves these problems with the 2T SC module and an artificial photosynthetic 2T-EC device.[28–32] In the VM module, multiple PVK SCs and Si SCs constitute the top and bottom modules, respectively, which are connected in parallel. Semi-transparent PVK SCs used in this configuration have been developed to be used for four-terminal (4T) tandem SCs and see-through SCs.[33,34] The numbers of the series-connected PVK and Si SCs in the top and bottom modules, respectively, are tuned so that the V_{MPP} values of these two modules are approximately the same as each other. Parallel connection of the top and bottom modules eliminates the current matching problem, leading to high robustness against solar spectrum variation. Instead, voltage matching is a unique requisite to the VM configuration for a high η_{SC}. More intense solar illumination increases V_{MPP}, whereas a higher temperature decreases V_{MPP}. These changes would break the voltage matching and consequently lower η_{SC} because the effects of the solar intensity and temperature on the PVK SCs and Si SCs are different from each other.

The artificial photosynthetic device with a VM-*n*EC configuration is displayed in Fig. 1(d), in which the VM tandem SC module powers the EC module. By tuning the series-connected SC numbers in the VM module and the number of EC reactors that are connected in series in the EC module, the V_{MPP} of the VM module per a single EC reactor is suitably set under a given condition. However, variations in the solar intensity and temperature affect the VM-*n*EC devices more detrimentally, as discussed below, than the VM SC modules coupled with power conditioners described above.

Figure 2 shows the J–V curves of an SC module with the load curve of an EC reactor. Under the condition used for optimization (tuning the series connection numbers for the VM-*n*EC device), V_{MPP} of the J–V curve of the solid line coincides with V_{op}, and hence J_{op} is close to the photocurrent density (J_{ph}). When the solar illumination becomes more intense, J_{ph} increases proportionally to the solar intensity, whereas V_{MPP} shifts higher only slightly [the broken line in Fig. 2(a)]. Therefore, V_{op} becomes larger than V_{MPP} and J_{op} smaller than J_{ph}, resulting in a notable lowering in η_{STC} that is proportional to J_{op}. On the other hand, under weaker solar illumination, η_{STC} scarcely changes because $J_{op} \cong J_{ph}$ holds [the dashed–dotted line in Fig. 2(a)]. However, V_{op} becomes smaller than V_{MPP}, in other words, the voltage loss increases

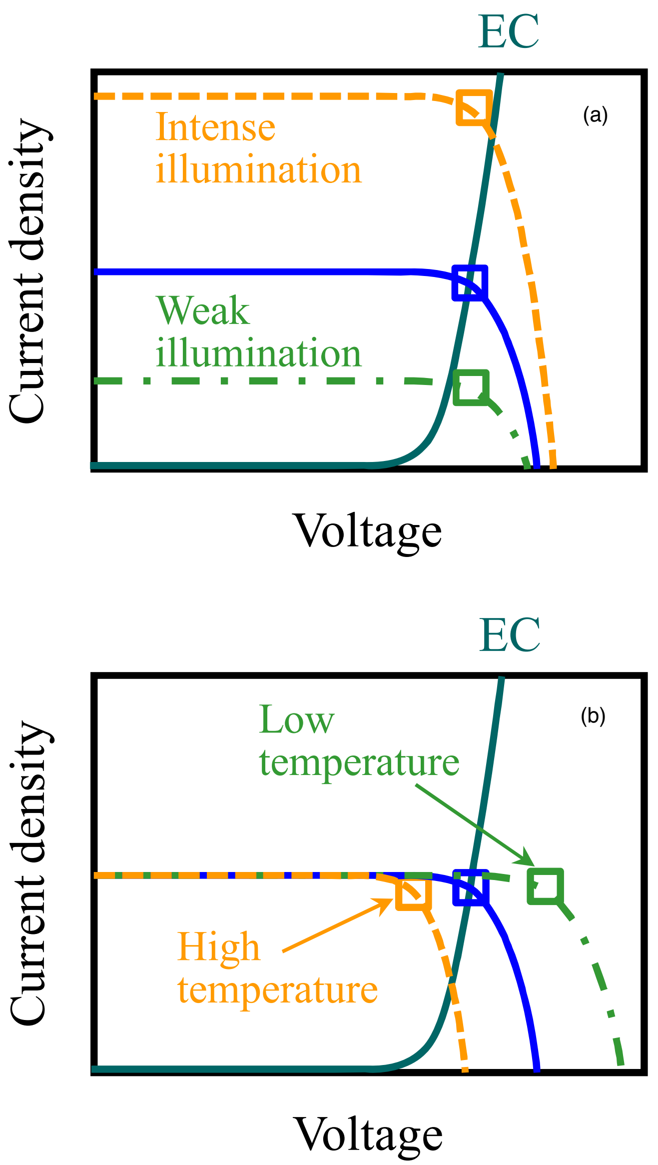

Fig. 2. Dependences on (a) the solar intensity and (b) the temperature of the current density–voltage (J–V) curve of an SC module. The open square indicates the maximal power point for each condition. The load curve of an EC module is also plotted. The intersection of the two curves determines the operating point (J_{op} and V_{op}).

because too many PVK and Si SCs are connected in series for this weaker solar illumination.

When the temperature rises, V_{MPP} decreases whereas J_{ph} does not change [the broken line in Fig. 2(b)]. Hence, V_{op} exceeds V_{MPP}, J_{op} decreases far below J_{ph}, and consequently η_{STC} notably lowers. A lower temperature also detrimentally affects η_{STC} because of a significant voltage loss [the dashed–dotted line in Fig. 2(b)].

The lowering in η_{STC} arising from the mismatch between V_{op} and V_{MPP} is unique to the present artificial photosynthetic devices, and is in contrast to that the power conditioner adjusts the load so that the SC module always operates at V_{MPP}. Therefore, the design guide should be clarified to mitigate these detriments.

A 4T tandem SC module in which the output powers of the top and bottom modules are extracted separately eliminates both the current matching and voltage matching problems. However, it has the drawback that a dual power converter or EC module must be connected because of the two different output voltages. Nevertheless, η_{SC} and η_{STC} using the 4T SC modules are virtually the same as those of the optimally designed VM SC modules (a single output with two terminals) and VM-nEC devices.[28,29,31,32] Therefore, the detailed evaluation on the 4T modules are described in Appendix A and excluded from the main considerations.

3. Modeling of photovoltaic processes and formulation of energy conversion efficiency

The objective of the present study is to clarify the design guide for VM-nEC artificial photosynthetic devices using PVK and Si SCs to minimize the detrimental impacts of varying solar intensity and temperature and to achieve high annual production. For this purpose, we modeled the J–V characteristics of the VM tandem SC modules. Then, we calculated η_{STC} for two kinds of artificial photosynthetic devices: H_2 production from H_2O and CO production from CO_2, and systematically investigated the impacts of the external operating conditions. Prior to consideration of these devices, η_{SC} values of the VM SC modules were also evaluated for clarifying the difference between the VM modules coupled with power conditioners and those combined with the EC modules. To capture the general trends rather than to precisely evaluate η_{SC} for a specific case, we constructed the following simplified models that describe the essence of the VM configuration.

3.1. Solar-to-electricity energy conversion efficiency of tandem SC modules (η_{SC})

The current density of a single-junction SC ($j^{(SC)}$) is described by the following formulation derived from an equivalent circuit model consisting of a constant current source, a diode, and a series resistance,[28,35,36]

$$j^{(SC)}[v] = j_{ph} - j_0\,(\exp[q\,(v + r_s\, j^{(SC)}[v])/k_B\, T_{cell}]), \quad (1)$$

where j_{ph}, j_0, and r_s are the current density, reverse saturation current density of the diode, and series resistance, respectively, and q, k_B, and T_{cell} denote the elementary charge, Boltzmann constant, and cell temperature, respectively. The external quantum efficiency (η_{EQE}) of the photovoltaic conversion can be approximated to be a constant independent of the photon energies, and then j_{ph} is determined from the bandgap (E_g) of the light-absorbing material used in the SC and the spectral photon flux of solar illumination ($n_{sun}[\hbar\omega]$),

$$j_{ph} = q\,\eta_{EQE}\int_{E_g}^{\infty} d(\hbar\omega)\, n_{sun}[\hbar\omega]. \quad (2)$$

For the Si bottom SC, the upper bound of the integration range in Eq. (2) is E_g of the top PVK SC ($E_g^{(PVK)}$). This means no overlap between the PVK and Si absorption ranges, and hence will lead to slight overestimations of η_{SC} and the impact of spectrum variation on η_{SC}. The component originating from the radiative recombination involved in the recombination current density in Eq. (1) is determined by the generalized Plank law.[37] In addition, the external radiative efficiency (η_{ERE}) is introduced for the expression of the nonradiative component.[36,38] Thus, by replacing the Fermi–Dirac distribution function with the

Boltzmann distribution function,

$$j_0 = \frac{2\,\pi\,k_B\,T_{cell}}{h^3\,c^2\,\eta_{ERE}}\,(E_g^2 + 2E_g\,T_{cell} + 2\,T_{cell}^2)\exp\left[-E_g/(k_B\,T_{cell})\right] \quad (3)$$

is derived, with h and c being the Plank constant and light velocity in vacuum, respectively.

The VM tandem SC module consists of the parallel-connected top module and bottom module, in which n_{PVK} PVK SCs and n_{Si} Si SCs are connected in series, respectively. The J–V relation per a single PVK SC is derived as follows,

$$J = j_{PVK}[V] + j_{Si}[V/(n_{Si}/n_{PVK})]/(n_{Si}/n_{PVK}). \quad (4)$$

It should be noted that the ohmic losses in the transparent electrodes and connecting wires and the photon losses arising from reflection and parasitic absorption that do not contribute to photovoltaic conversion are neglected.

The J–V characteristics of the 2T tandem SC module are obtained by solving the simultaneous equation,

$$\begin{cases} J = j_{top}[v_{top}] = j_{bot}[v_{bot}] \\ V = v_{top} + v_{bot} \end{cases}. \quad (5)$$

When the SC module is coupled with a power conditioner, η_{SC} is the ratio of the maximal value of the output power density that is equal to the product of J and V as a function of V to the solar intensity (P_{sun}),

$$\eta_{SC} = J[V]\cdot V|_{max}/P_{sun}. \quad (6)$$

For numerical evaluations, η_{EQE}, η_{ERE}, and r_s for the PVK and Si SCs were determined so that the photovoltaic properties calculated using Eq. (1) are approximately the same as the values of the world-record SCs measured under the standard condition for SC evaluation of the AM 1.5 G illumination (P_{sun} = 100 mW cm^{-2})[39] and T_{cell} = 25 °C: $\eta_{EQE} = 0.90$, $\eta_{ERE} = 0.15$, and $r_s = 3.1\ \Omega\ \mathrm{cm}^2$ for the PVK SC ($E_g^{(PVK)} = 1.51$ eV); and $\eta_{EQE} = 0.96$, $\eta_{ERE} = 0.0062$, and $r_s = 0.28\ \Omega\ \mathrm{cm}^2$ for the heterojunction (HJ) Si SC. These parameter sets reproduce the experimental results well, as summarized in Table I.[17,40] Although more complicated equivalent circuits including the diode ideal factor and two diodes have been proposed for more precise fitting,[41,42] Eq. (1) well describes the J–V characteristics of a highly efficient SC at around its maximal power point, which fits the objective of the present study. For the PVK SCs with different $E_g^{(PVK)}$ values, the same parameter set was used neglecting the $E_g^{(PVK)}$-dependence. This approximation leads to a higher η_{SC} than those previously demonstrated at a wider $E_g^{(PVK)}$. For example, η_{SC} = 23.8% at $E_g^{(PVK)}$ = 1.7 eV is higher than the record efficiency of 22% using metal electrodes[43] and 20% of semi-transparent SCs with $E_g^{(PVK)}$ = 1.6 eV,[34,44] and therefore would be a target value.

When an SC operates outdoors, T_{cell} changes. A higher T_{cell} narrows E_g and hence increases j_{ph}. However, the detriments of a smaller open-circuit voltage and a lower filling factor arising from more significant radiative and nonradiative recombination surpass the benefit of the larger j_{ph}. Consequently, η_{SC} lowers. Thus, the dependences of η_{SC} and η_{STC} on T_{cell} are essential for evaluation of annual production.[31,45,46] Therefore, the explicit T_{cell} dependence and T_{cell}-dependent E_g (dE_g/dT_{cell} = 0.31 meV K^{-1} for PVK[47] and −0.27 meV K^{-1} for Si[48]) in Eqs. (1)–(3) are involved, whereas η_{EQE}, η_{ERE}, and r_s are approximated to be constant independent of T_{cell}. The resultant T_{cell}-dependences of η_{SC}, i.e. $d\eta_{SC}/dT_{cell}$ is −0.15% K^{-1} for the PVK SC and −0.27% K^{-1} for the Si SC, are close to the experimental values of −0.17% K^{-1} (PVK)[49] and −0.26% K^{-1} (HJ Si).[50]

3.2. Solar-to-H_2 and -CO energy conversion efficiencies of artificial photosynthetic devices (η_{H2} and η_{CO})

The operating point of the VM-nEC artificial photosynthetic device illustrated in Fig. 1(d) is determined from the J–V curve of the VM tandem SC module and the load curve of the EC module. When n_{EC} EC reactors are connected in series in the EC module powered by the VM SC module, the J–V curve per a single EC reactor is

$$J = j_{PVK}[V/(n_{PVK}/n_{EC})]/(n_{PVK}/n_{EC}) + j_{Si}[V/(n_{Si}/n_{EC})]/(n_{Si}/n_{EC}). \quad (7)$$

The intersection of this J–V curve and the load curve of the EC reactor ($j_{EC}[V]$) determines the operating point (J_{op} and V_{op}).

The Faradaic efficiency (η_{FE}) of the EC reaction of $H_2O \rightarrow H_2 + 1/2\ O_2$ is virtually unity. The thermodynamic threshold voltage of this reaction is 1.23 V. Thus, the conversion efficiency of solar energy to chemical energy of H_2 (η_{H2}) is derived as follows,

$$\eta_{H2} = 1.23\ J_{op}/P_{sun}. \quad (8)$$

On the other hand, η_{FE} of the $CO_2 \rightarrow CO + 1/2\ O_2$ reaction is lower than unity and dependent on V_{op}. Therefore, the solar-to-CO energy conversion efficiency (η_{CO}) is calculated by

$$\eta_{CO} = 1.34\ J_{op}\ \eta_{FE}[V_{op}]/P_{sun} \quad (9)$$

using the thermodynamic threshold voltage of 1.34 V.

For numerical evaluations, the load curve of the H_2-producing reactor was taken from Ref. 51, the load curve and η_{FE} for the CO production from Ref. 52, and these curves are depicted in Fig. 3. CO production requires a higher voltage by approximately 0.2 V than H_2 production. Another point is that the η_{FE} of CO production lowers with decreasing voltage from 1.7 V.

Table I. Comparison between the calculated (calc.) values and experimental (expt.) results of the short-circuit current density (j_{SC}), open-circuit voltage (v_{OC}), filling factor (ff), and energy conversion efficiency (η_{SC}) of the PVK and heterojunction Si SCs.

		j_{SC} (mA/cm^2)	v_{OC} (V)	ff	η_{SC} (%)
PVK	Calc.	25.8	1.189	0.833	25.5
(E_g = 1.51 eV)	Expt.[a]	25.7	1.189	0.832	25.5
Heterojunction Si	Calc.	42.1	0.744	0.838	26.2
(E_g = 1.12 eV)	Expt.[b]	41.8	0.744	0.838	26.3

a) Ref. 17. b) Ref. 40.

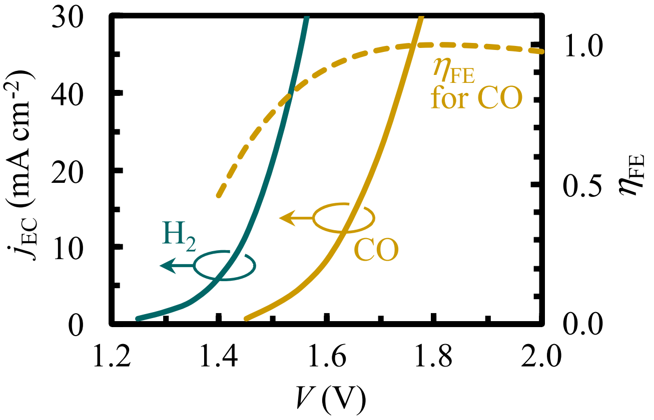

Fig. 3. Load curve of an H_2-producing EC reactor,[51] and the load curve and voltage-dependent η_{FE} of a CO-producing EC reactor.[52]

3.3. Outdoor operation conditions

The standard condition for SC evaluations is the combination of AM 1.5 G illumination (P_{sun} = 100 mW cm^{-2})[39] and T_{cell} = 25 °C. However, this is a rare condition for outdoor use; mostly, P_{sun} is smaller and T_{cell} is higher. Therefore, the average values of P_{sun} and T_{cell} ($\langle P_{sun}\rangle$ and $\langle T_{cell}\rangle$, respectively) and their distributions were obtained for a south-facing 32° slope using a database of P_{sun}, solar spectrum, and ambient temperature (T_a) measured in Tsukuba, Japan (N36° and E140°, in 2015).[53] The weighted values of $\langle P_{sun}\rangle$ and $\langle T_{cell}\rangle$ by P_{sun} were calculated as follows because the electricity of the SC modules and the H_2 and CO production rates of the artificial photosynthetic devices are approximately proportional to P_{sun},

$$\langle P_{sun}\rangle = \int dt\, P_{sun}^2[t] \Big/ \int dt'\, P_{sun}[t'], \tag{10}$$

$$\langle T_{cell}\rangle = \int dt\, T_{cell}[t]\, P_{sun}[t] \Big/ \int dt'\, P_{sun}[t']. \tag{11}$$

An empirical relation of P_{sun} and T_a to T_{cell} was adopted for determining T_{cell},[49]

$$T_{cell} = (NOCT - 20[°C])\, P_{sun}/80\,[\mathrm{mW\,cm^{-2}}] + T_a, \quad NOCT = 44\,°C, \tag{12}$$

where $NOCT$ denotes the nominal operating cell temperature defined as T_{cell} at P_{sun} = 80 mW cm^{-2}, T_a = 20 °C, and a wind speed of 1 m s^{-1}.

The results were $\langle P_{sun}\rangle$ = 63.9 mW cm^{-2} and $\langle T_{cell}\rangle$ = 37.7 °C, and their distributions are depicted in Figs. 4(a) and 4(b), respectively. Eighty percent of the relative frequency distribution of P_{sun} locates in a range of 20–95 mW cm^{-2}, and 80% of the T_{cell} distribution in 20 °C–55 °C.

The average of $n_{sun}[\hbar\omega]$ ($\langle n_{sun}[\hbar\omega]\rangle$) was determined in a similar manner,

$$\langle n_{sun}[\hbar\omega]\rangle = \int dt\, n_{sun}[\hbar\omega, t]\, P_{sun}[t] \Big/ \int dt'\, P_{sun}[t']. \tag{13}$$

As is clear from Figs. 4(c) and 4(d), $\langle n_{sun}[\hbar\omega]\rangle$ is close to the AM 1.5 G photon flux, except that the high photon-energy components are relatively only slightly more intense. The variation in the spectrum was quantified by the relative difference ($\Delta\tilde{j}_{ph}$) between the photocurrent densities of the PVK with $E_g^{(PVK)}$ = 1.7 eV and Si SCs ($j_{ph}^{(PVK)}$ and $j_{ph}^{(Si)}$, respectively),

$$\Delta\tilde{j}_{ph} = 2\,(j_{ph}^{(PVK)} - j_{ph}^{(Si)}) \big/ (j_{ph}^{(PVK)} + j_{ph}^{(Si)}). \tag{14}$$

The frequency distribution of $\Delta\tilde{j}_{ph}$ is depicted in Fig. 4(e); 80% of the relative distribution ranges from −0.05 to 0.2 with $\Delta\tilde{j}_{ph}$ = 0.036 for $\langle n_{sun}[\hbar\omega]\rangle$.

Although the characteristics of the EC reactors are also affected by their temperature, the general trends are not clear because the effects differ depending on the target reactions and catalyst materials.[54,55] In addition, the temperature variation is smaller than that of the SC module that is directly solar-illuminated. Therefore, the temperature dependence was neglected, and j_{EC} and η_{FE} measured at RT, shown in Fig. 3, were always used.

Recently, high-performance PVK SCs with up to $E_g^{(PVK)}$ = 1.7 eV have been realized.[15,16] Therefore, we employed a combination of the Si SCs and PVK SCs with $E_g^{(PVK)}$ = 1.7 eV to design the VM tandem SC modules and artificial photosynthetic VM-nEC devices. First, n_{Si}/n_{PVK} of the VM module was optimized so that η_{SC} was maximized under the "average" condition of $\langle P_{sun}\rangle$, $\langle T_{cell}\rangle$, and $\langle n_{sun}[\hbar\omega]\rangle$ derived above, and subsequently other practical conditions depicted in Fig. 4. Although n_{PVK} and n_{Si} are integers, n_{Si}/n_{PVK} can be finely tuned for a large-sized module with large n_{PVK} and n_{Si}. Therefore, they were dealt with as continuous variables. Then, the annually averaged η_{SC} ($\eta_{SC}^{(annual)}$) determined by the ratio of the accumulated electricity production to the accumulated solar intensity was calculated. Thus, the suitable optimization condition was sought by investigating the impacts of the optimization conditions on $\eta_{SC}^{(annual)}$. The design parameters of the artificial photosynthetic devices, i.e. n_{PVK}/n_{EC} and n_{Si}/n_{EC}, were similarly dealt with as continuous variables and optimized. The effects of the optimization conditions on the annually averaged η_{H2} and η_{CO} ($\eta_{H2}^{(annual)}$ and $\eta_{CO}^{(annual)}$, respectively) were investigated, and thus the design guide was derived. Finally, we discussed the feasibility of improvements in $\eta_{SC}^{(annual)}$, $\eta_{H2}^{(annual)}$, and $\eta_{CO}^{(annual)}$ assuming realization of PVK SCs with $E_g^{(PVK)}$ wider than 1.7 eV, by calculating $\eta_{SC}^{(annual)}$, etc. as functions of $E_g^{(PVK)}$.

4. Results and discussion

4.1. VM tandem SC modules

First, we considered the VM tandem SC modules illustrated in Fig. 1(c). Figure 5(a) shows the dependence of η_{SC} on P_{sun} for the VM module (n_{Si}/n_{PVK} = 1.98) optimized under the average condition of $\langle P_{sun}\rangle$ = 63.9 mW cm^{-2}, $\langle T_{cell}\rangle$ = 37.7 °C, and $\langle n_{sun}[\hbar\omega]\rangle$ ($\Delta\tilde{j}_{ph}$ = 0.036). The V_{MPP} values of the VM module and top/bottom modules are also depicted. In the calculated P_{sun} range, V_{MPP} of the Si SC monotonically increases, proportionally to log [P_{sun}]. By contrast, the V_{MPP} of the PVK SC changes only slightly, because its r_s is an order of magnitude larger than that of the Si SC and hence the ohmic loss is more significant at a large P_{sun}.[56,57] As a result, the change in η_{SC} is 0.9% at most in the P_{sun} range of 20–95 mW cm^{-2} in which the relative frequency distribution accounts for 80%. Although the difference between the V_{MPP} values of the PVK and Si SCs, namely, the voltage mismatch, increases when P_{sun} shifts from $\langle P_{sun}\rangle$, it is as small as 0.05 V at most in the relevant P_{sun} range. Thus, it causes only a slight lowering in η_{SC}, smaller than 0.2% at a given P_{sun} relative

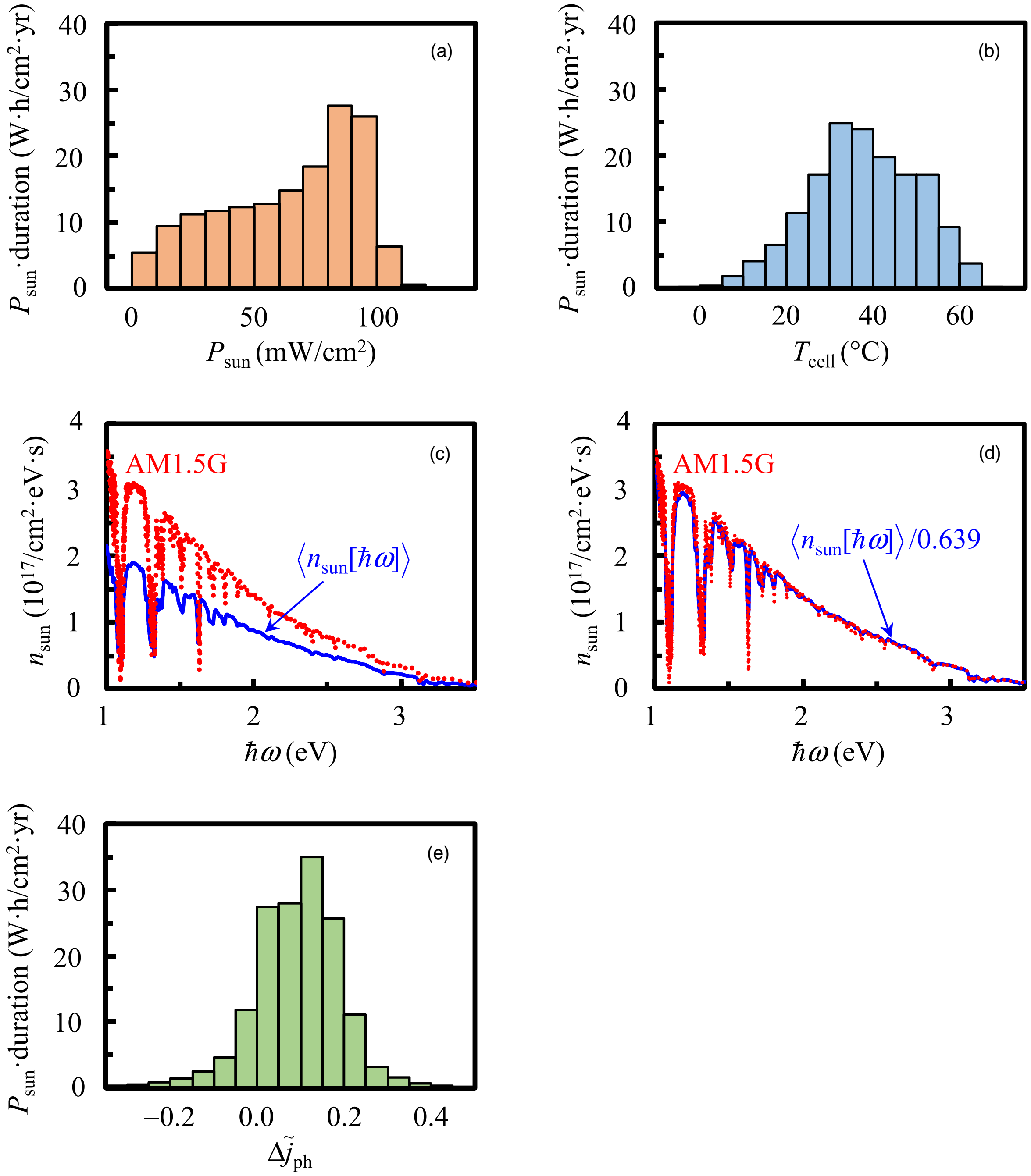

Fig. 4. Frequency distributions of (a) the solar intensity (P_{sun}) and (b) cell temperature (T_{cell}). (c) and (d) Annually averaged spectral solar photon flux ($\langle n_{sun}[\hbar\omega]\rangle$) compared with the AM 1.5 G spectrum. Converted $\langle n_{sun}[\hbar\omega]\rangle$ corresponding to $P_{sun} = 100$ mW cm^{-2} is plotted in (d) for direct comparison with the AM 1.5 G. (e) Frequency distribution of the relative difference in the photocurrent densities ($\Delta\tilde{j}_{ph}$). P_{sun} and $n_{sun}[\hbar\omega]$ were measured on a south-facing 32° slope in Tsukuba, Japan (N36° and E140°, in 2015),[53] whereas T_{cell} was estimated from the measured P_{sun} and ambient temperature (T_a) using Eq. (12).

to that of the 4T tandem SC that is free from the voltage mismatching problem. The details are discussed in Appendix A.

By contrast, the impact of T_{cell} is notable, as is clear from Fig. 5(b). When T_{cell} rises from the lower bound (20 °C) to the upper bound (55 °C) of 80% of the relative frequency distribution, η_{SC} lowers by 2.2% because the V_{MPP} of each submodule is a decreasing function of T_{cell}. In addition, the V_{MPP} of the Si SC decreases more rapidly than that of the PVK SC. However, the detrimental impact of the resultant voltage mismatch is marginal. The maximal mismatch is 0.04 V, which lowers η_{SC} relative to that of the 4T module by only 0.2%.

On the other hand, it is apparent that the impact of $\Delta\tilde{j}_{ph}$ is extremely weak, as shown in Fig. 5(c), even though the present model of no overlap between the PVK and Si absorption ranges would overestimate the impact. The voltage mismatch is 0.005 V at most, corresponding to a negligibly small change in η_{SC} of 0.0002%, in the $\Delta\tilde{j}_{ph}$ range of the 80% frequency distribution between −0.05 to 0.2.

Thus, it was found that the impact of T_{cell} on η_{SC} is notable, whereas the other two operating conditions of P_{sun} and $n_{sun}[\hbar\omega]$ have only a slight effect. Therefore, n_{Si}/n_{PVK} was optimized under three T_{cell} conditions: $T_{cell} = 25$ °C, $\langle T_{cell}\rangle = 37.7$ °C, and 50 °C with the average conditions for P_{sun} and $n_{sun}[\hbar\omega]$. The results are compared in Fig. 6. Although the slope of the η_{SC} vs. T_{cell} relation depends on the T_{cell} value adopted for the optimization, the difference is minor.

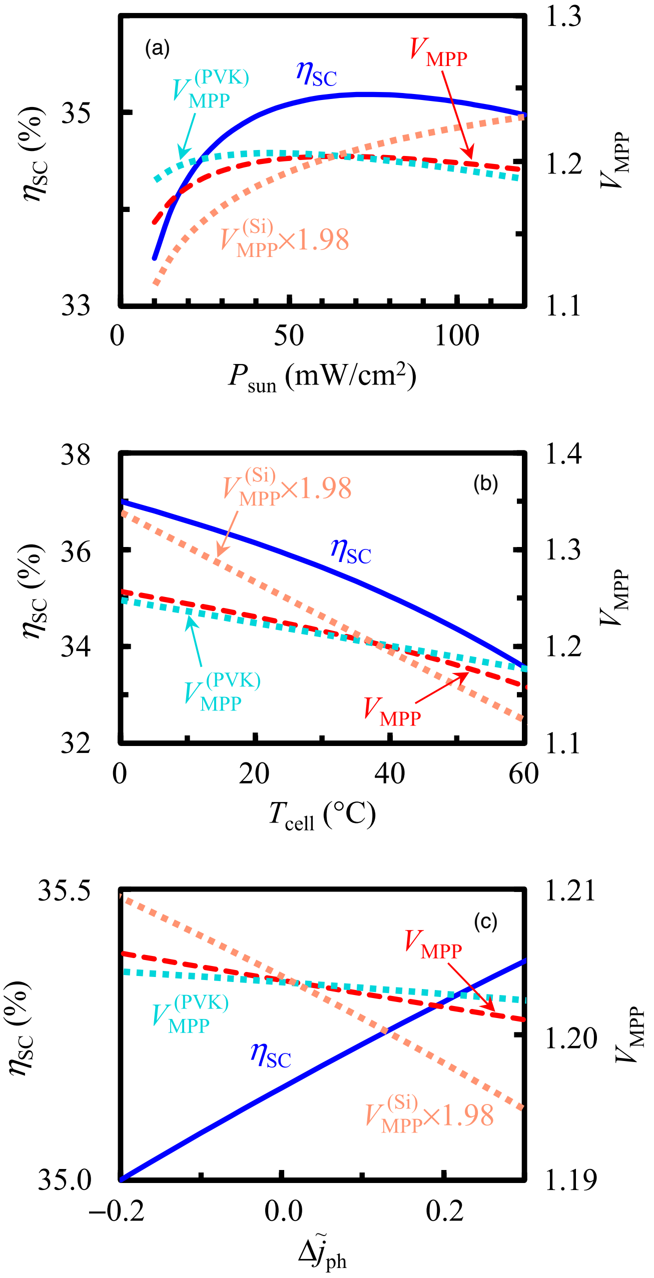

Fig. 5. η_{SC} and V_{MPP} of the VM tandem SC module and V_{MPP} values of the top/bottom modules. The optimization conditions are the average conditions of $P_{sun} = \langle P_{sun} \rangle = 63.9$ mW cm^{-2}, $T_{cell} = \langle T_{cell} \rangle = 37.7$ °C, and $n_{sun}[\hbar\omega] = \langle n_{sun}[\hbar\omega] \rangle$ ($\Delta\tilde{j}_{ph} = 0.036$), resulting in $n_{Si}/n_{PVK} = 1.98$. The operating conditions are the average conditions except for the parameter of the horizontal axis in each figure.

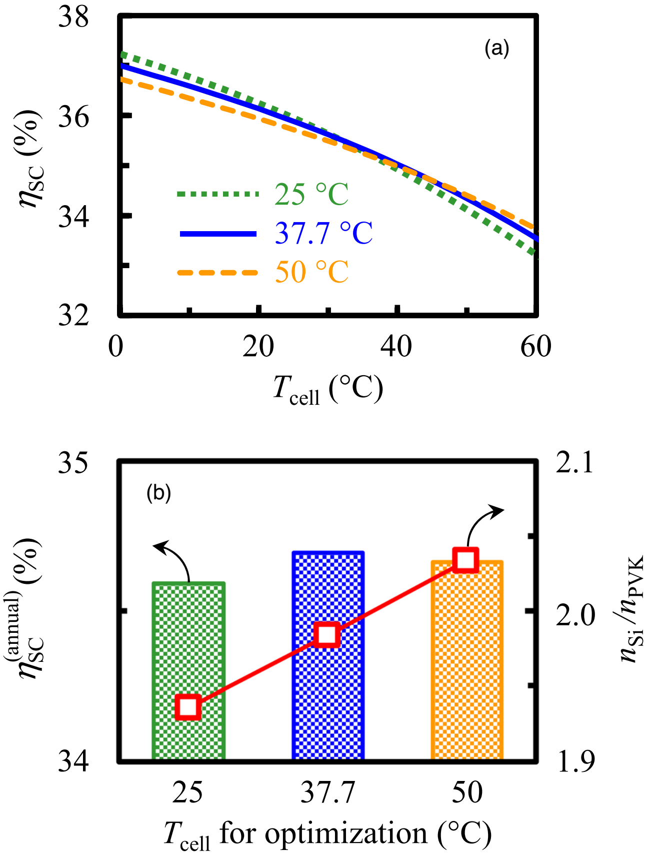

Fig. 6. (a) η_{SC} of the VM tandem SC modules optimized under the conditions of $P_{sun} = \langle P_{sun} \rangle$, $T_{cell} = 25$ °C, $\langle T_{cell} \rangle = 37.7$ °C, and 50 °C, and $n_{sun}[\hbar\omega] = \langle n_{sun}[\hbar\omega] \rangle$. The operating conditions are the average conditions except T_{cell}. (b) Impact of T_{cell} used for the optimization of n_{Si}/n_{PVK} on $\eta_{SC}^{(annual)}$.

Consequently, all three $\eta_{SC}^{(annual)}$ values, which are the average of η_{SC} over various T_{cell} values, are almost the same: 34.6%–34.7%. In other words, $\eta_{SC}^{(annual)}$ is scarcely affected even when the design parameter of n_{Si}/n_{PVK} changes between 1.9–2.0. Further, when n_{Si}/n_{PVK} was optimized under the condition of the AM 1.5 G illumination ($P_{sun} = 100$ mW cm^{-2}) and $T_{cell} = 25$ °C that is the standard for SC evaluation, $\eta_{SC}^{(annual)}$ was 34.5%, virtually the same as the abovementioned three values. The resultant $\eta_{SC}^{(annual)}$ values are more realistic than the results of over 40% in the radiative limit,[29] although there remains a slight discrepancy from the practically achievable values because the parasitic optical and ohmic losses are neglected in the present model as described in Sect. 3.1. In addition, improvements in semi-transparent PVK SCs are obviously essential.

Consequently, n_{Si}/n_{PVK} of the VM tandem SC module can be optimized under any practical conditions. This is because the lowering in η_{SC} caused by the voltage mismatch under varying operation conditions is smaller than 0.2% in most cases, and hence scarcely affects η_{SC} in the annual average. This is also the reason that $\eta_{SC}^{(annual)} = 34.7\%$ of the 4T tandem SC module calculated in a similar manner is almost the same as that of the VM module. A detailed comparison between the VM module and 4T module is described in Appendix A.

4.2. VM-*n*EC H_2-producing artificial photosynthetic devices

Next, we calculated η_{H2} of the H_2-producing artificial photosynthetic devices consisting of the VM tandem SC modules and EC modules shown in Fig. 1(d). The requisite for a high η_{H2} is that the V_{MPP} of the SC module is a little larger than 1.4 eV, as stated in Sect. 2. Figure 7 depicts the results for the device optimized under the average condition ($n_{PVK}/n_{EC} = 1.22$ and $n_{Si}/n_{EC} = 2.43$). The significant difference from η_{SC} of the VM SC module coupled with a power conditioner displayed in Fig. 5 is that η_{H2} is a monotonically decreasing function of P_{sun}. The lowering in η_{H2} is as large as 1.6% when P_{sun} increases from 20 mW cm^{-2} to 95 mW cm^{-2}. Another difference is that η_{H2} becomes only slightly higher at a lower T_{cell} than

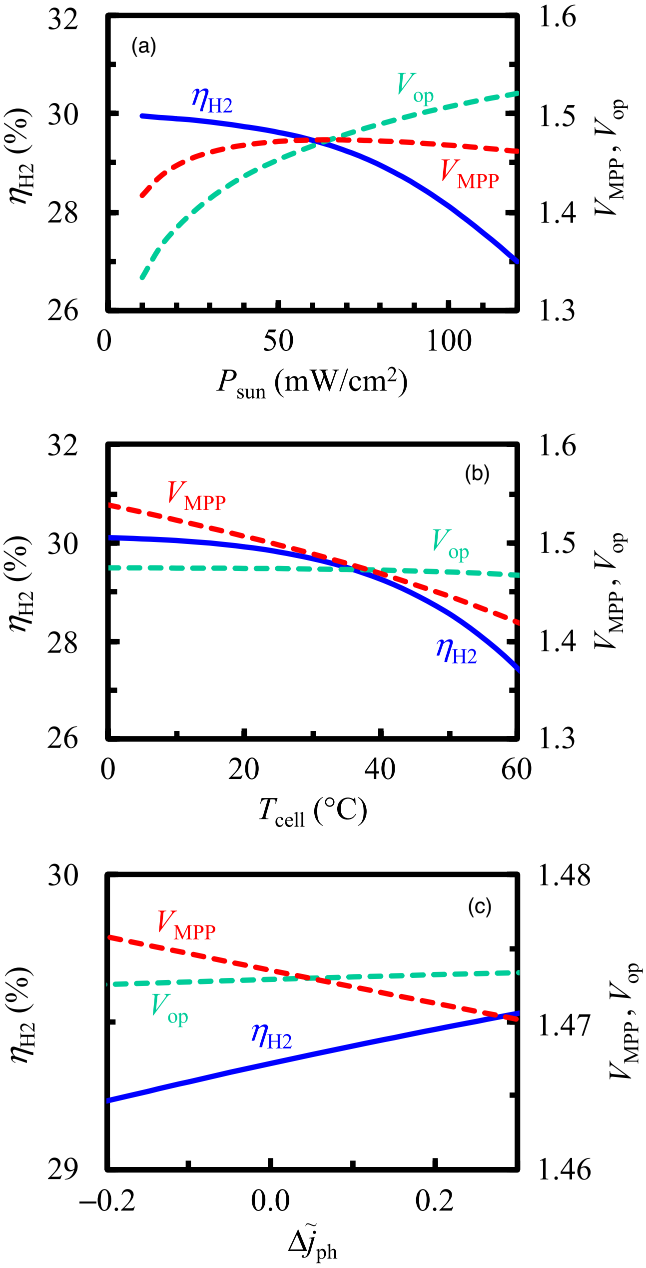

Fig. 7. η_{H2} and V_{op} of the VM-nEC H_2-producing artificial photosynthetic device, and V_{MPP} of the VM tandem SC module used in the device. The optimization conditions are the average conditions of $P_{sun} = \langle P_{sun} \rangle = 63.9$ mW cm^{-2}, $T_{cell} = \langle T_{cell} \rangle = 37.7$ °C, and $n_{sun}[\hbar\omega] = \langle n_{sun}[\hbar\omega] \rangle$ ($\Delta\tilde{j}_{ph} = 0.036$), resulting in $n_{PVK}/n_{EC} = 1.22$ and $n_{Si}/n_{EC} = 2.43$. The operating conditions are the average conditions except for the parameter of the horizontal axis in each figure.

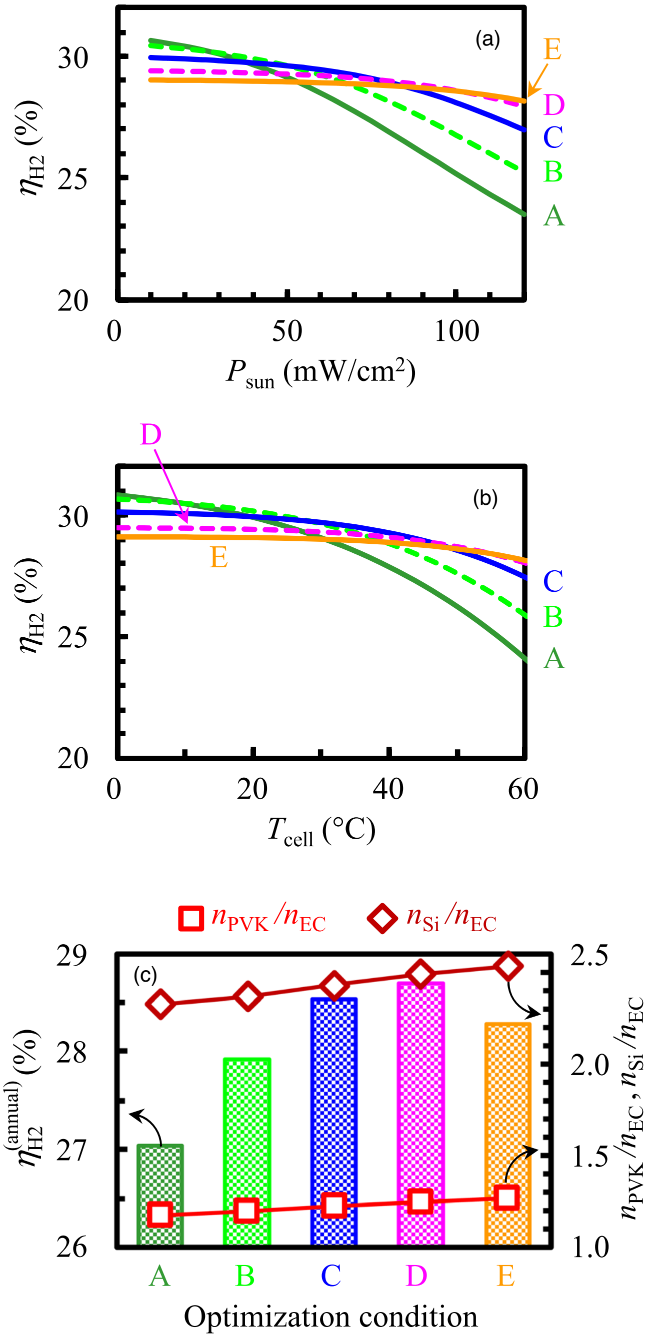

Fig. 8. (a) and (b) η_{H2} of the VM-nEC H_2-producing artificial photosynthetic devices optimized under five conditions, A–E. A: $P_{sun} = 40$ mW cm^{-2} and $T_{cell} = 25$ °C. B: $P_{sun} = 50$ mW cm^{-2} and $T_{cell} = 30$ °C. C: $P_{sun} = \langle P_{sun} \rangle = 63.9$ mW cm^{-2} and $T_{cell} = \langle T_{cell} \rangle = 37.7$ °C. D: $P_{sun} = 80$ mW cm^{-2} and $T_{cell} = 45$ °C. E: $P_{sun} = 90$ mW cm^{-2} and $T_{cell} = 50$ °C. $n_{sun}[\hbar\omega] = \langle n_{sun}[\hbar\omega] \rangle$ is used for the optimization for all conditions A–E. The operating conditions are the average conditions except for the parameter of the horizontal axis in each figure. (c) Impacts of P_{sun} and T_{cell} used for the optimization of n_{PVK}/n_{EC} and n_{Si}/n_{EC} on $\eta_{H2}^{(annual)}$.

$\langle T_{cell} \rangle = 37.7$ °C although the lowering in the higher T_{cell} range is similar to that for η_{SC}. On the other hand, the effect of $\Delta\tilde{j}_{ph}$ is again marginal.

These dependences of η_{H2} on P_{sun} and T_{cell} arise from the mismatch between V_{MPP} of the SC module and V_{op}, as depicted in Fig. 2. A larger P_{sun} and a higher T_{cell} lead to $V_{MPP} < V_{op}$, and therefore η_{H2} that is proportional to J_{op}/P_{sun} rapidly lowers. On the other hand, when P_{sun} increases and T_{cell} falls, V_{op} decreases below V_{MPP}, J_{op} shifts from J_{MPP} toward J_{ph}, and consequently η_{H2} increases slightly.

Thus, P_{sun} and T_{cell} strongly affect η_{H2}; a large P_{sun} is equivalent to a high T_{cell}. Therefore, n_{PVK}/n_{EC} and n_{Si}/n_{EC} were optimized under five conditions in which both P_{sun} and T_{cell} were simultaneously changed. The results are shown in Fig. 8. When a small P_{sun} and a low T_{cell} are adopted for the optimization, η_{H2} lowers remarkably with increasing P_{sun} and T_{cell} although η_{H2} is high at a small P_{sun} and a low T_{cell}. By contrast, η_{H2} changes moderately when the design parameters of n_{PVK}/n_{EC} and n_{Si}/n_{EC} are optimized under a condition of a large P_{sun} and a high T_{cell}. Reflecting these trends, $\eta_{H2}^{(annual)}$ notably depends on the optimization conditions, in contrast to $\eta_{SC}^{(annual)}$. The best optimization condition, i.e. $P_{sun} = 80$ mW cm^{-2} and

$T_{cell} = 45$ °C (Condition D in Fig. 8) are both slightly greater than the average values. The maximal $\eta_{H2}^{(annual)}$ is as high as 28.7%, although there is a slight discrepancy from the practically achievable values, as discussed in Sect. 4.1. However, it should be noted that too large a P_{sun} and too high a T_{cell} (Condition E) decrease $\eta_{H2}^{(annual)}$.

When the device is optimized under the standard condition for SC evaluation of AM 1.5 G illumination ($P_{sun} = 100$ mW cm^{-2}) and $T_{cell} = 25$ °C, the resultant $\eta_{H2}^{(annual)} = 28.4\%$ is approximately the same as the maximal value determined under the best optimization condition. However, this is attributed to the combination of a P_{sun} close to the upper bound of the measured frequency distribution and a T_{cell} close to the lower bound shown in Fig. 4 having an effect similar to that of the best optimization condition, because a large P_{sun} is equivalent to a high T_{cell}. It should be noted again that the standard condition are far from typical conditions or the average condition.

Figure 9 compares the J–V curves of the VM tandem SC module used in the device optimized under the best optimization condition (Condition D in Fig. 8) with the load curve of the EC reactor. When the device operates under the optimization condition (the solid line), V_{op} determined by the intersection of the two curves, coincides with V_{MPP}, leading to a high η_{H2}. However, V_{op} shifts away from V_{MPP} and hence η_{H2} lowers when P_{sun} and T_{cell} change, although these detriments are minimized. This drawback of the direct connection of the SC module and EC module is solved by using a DC–DC converter for connecting these two modules. However, it is found that the energy loss originating from the voltage mismatch for the optimized device is smaller than the internal loss of a commonly used DC–DC converter with an efficiency of 90%–95%.[58,59] In short, the direct connection yields a higher $\eta_{H2}^{(annual)}$. The details are discussed in Appendix B.

4.3. VM-*n*EC CO-producing artificial photosynthetic devices

We also considered the CO-producing artificial photosynthetic devices. Figure 10 shows η_{CO}, V_{op}, and V_{MPP} of the device optimized under the average condition ($n_{PVK}/n_{EC} = 1.34$ and $n_{Si}/n_{EC} = 2.78$). As is clear from Fig. 10(a), η_{CO} rapidly lowers with decreasing P_{sun}. This qualitative difference from the P_{sun} dependence of η_{H2} depicted in Fig. 7(a) arises from the η_{FE} of the EC reactor that lowers at a low V_{op} and a small J_{op}; see Fig. 3. The hypothetical η_{CO} supposing $\eta_{FE} = 1$ (dotted line) depends on P_{sun} similarly to η_{H2}.

The impacts of the optimization conditions on the P_{sun}- and T_{cell}-dependent η_{CO} depicted in Figs. 11(a) and 11(b), respectively, are also similar to those for the H_2-producing devices, except for the rapid lowering in the small P_{sun} range arising from the low η_{FE}; see Fig. 8. Thus, $\eta_{CO}^{(annual)}$ is also maximized when the design parameters of n_{PVK}/n_{EC} and n_{Si}/n_{EC} are optimized

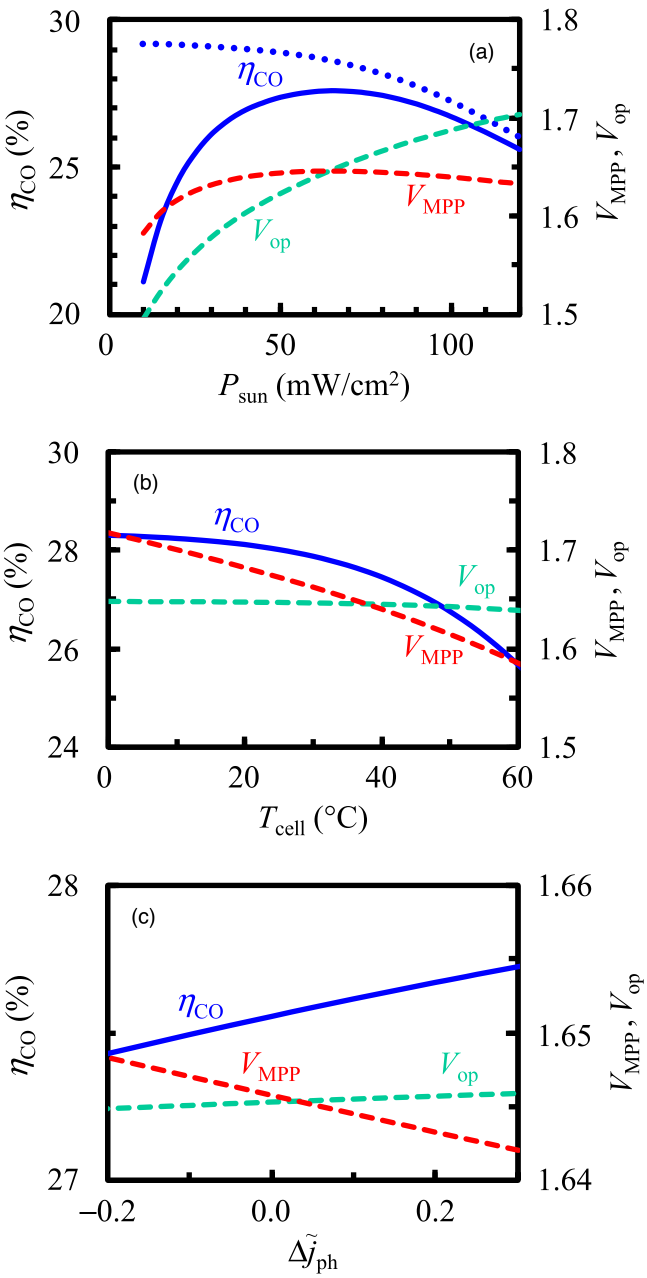

Fig. 10. η_{CO} and V_{op} of the VM-*n*EC CO-producing artificial photosynthetic device, and V_{MPP} of the VM tandem SC module used in the device. The optimization conditions are the average conditions of $P_{sun} = \langle P_{sun} \rangle = 63.9$ mW cm^{-2}, $T_{cell} = \langle T_{cell} \rangle = 37.7$ °C, and $n_{sun}[\hbar\omega] = \langle n_{sun}[\hbar\omega] \rangle$ ($\Delta\tilde{j}_{ph} = 0.036$), resulting in $n_{PVK}/n_{EC} = 1.34$ and $n_{Si}/n_{EC} = 2.78$. The operating conditions are the average conditions except for the parameter of the horizontal axis in each figure. The dotted line in (a) depicts η_{CO} supposing $\eta_{FE} = 1$.

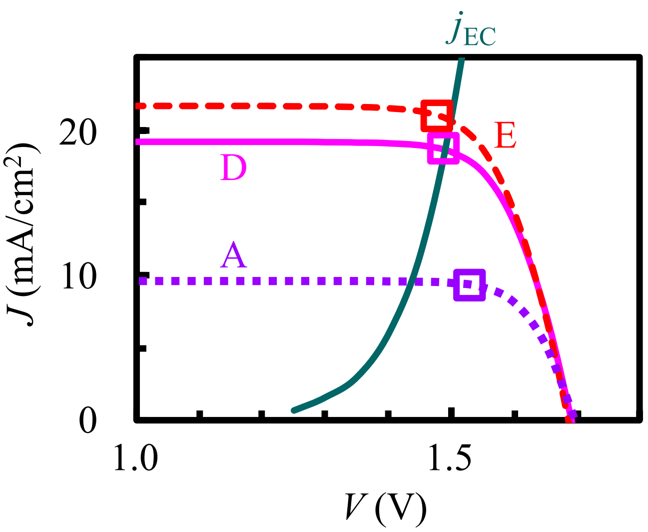

Fig. 9. J–V curves of the VM tandem SC module and the load curve of the EC module used in the VM-*n*EC H_2-producing artificial photosynthetic device. The optimization condition is D used in Fig. 8, and the operating conditions are A, D, and E. The open square depicts V_{MPP} under each operating condition.

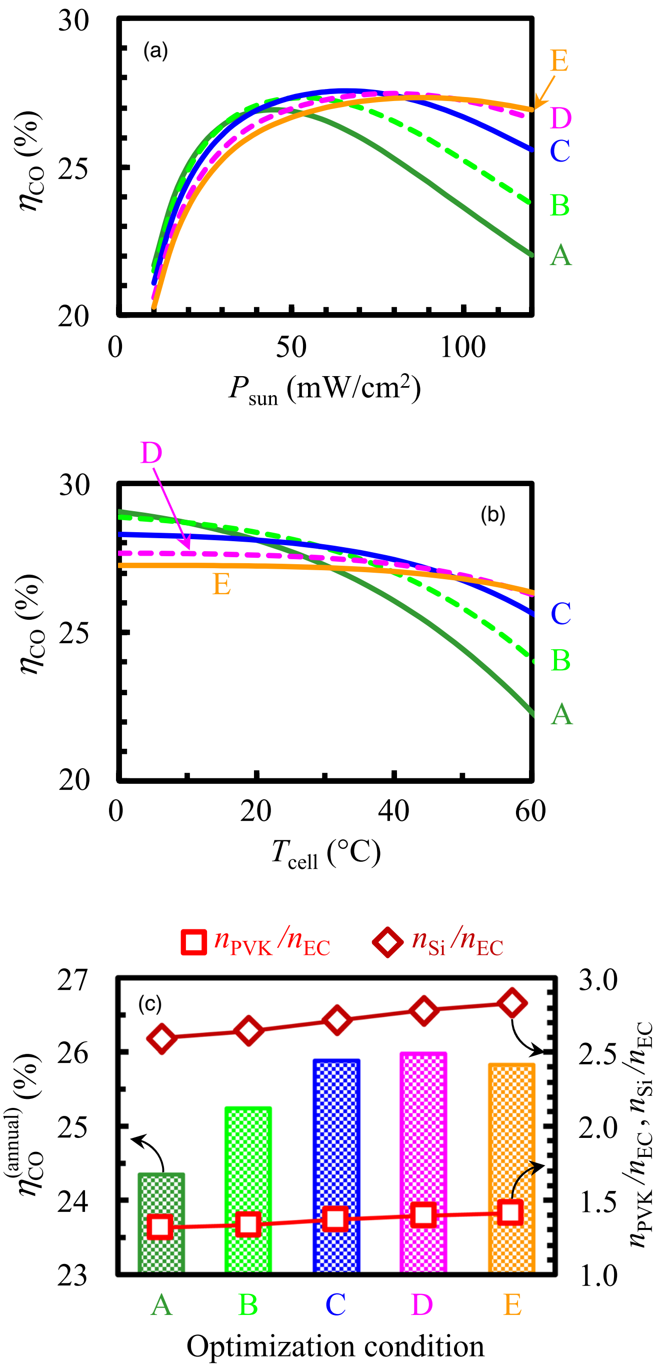

Fig. 11. (a) and (b) η_{CO} of the VM-nEC CO-producing artificial photosynthetic devices are optimized under five conditions, A–E. A: $P_{sun} = 40$ mW cm^{-2} and $T_{cell} = 25$ °C. B: $P_{sun} = 50$ mW cm^{-2} and $T_{cell} = 30$ °C. C: $P_{sun} = \langle P_{sun} \rangle = 63.9$ mW cm^{-2} and $T_{cell} = \langle T_{cell} \rangle = 37.7$ °C. D: $P_{sun} = 80$ mW cm^{-2} and $T_{cell} = 45$ °C. E: $P_{sun} = 90$ mW cm^{-2} and $T_{cell} = 50$ °C. $n_{sun}[\hbar\omega] = \langle n_{sun}[\hbar\omega] \rangle$ is used for the optimization for all conditions A–E. The operating conditions are the average conditions except for the parameter of the horizontal axis in each figure. (c) Impacts of P_{sun} and T_{cell} used for the optimization of n_{PVK}/n_{EC} and n_{Si}/n_{EC} on $\eta_{CO}^{(annual)}$.

under the condition of $P_{sun} = 80$ mW cm^{-2} and $T_{cell} = 45$ °C (Condition D in Fig. 11) that are both slightly greater than the average values. However, the lowering in $\eta_{CO}^{(annual)}$ when optimized with the larger P_{sun} and higher T_{cell} (Condition E) is moderate, reflecting that a smaller P_{sun} and a resultant smaller J_{op} lead to a lower η_{FE}. Therefore, the more precisely selected best P_{sun} for the optimization should be larger than that for the H_2 production. It should be again noted that the present model of the SC modules will slightly overestimate $\eta_{CO}^{(annual)}$.

The J–V curves of the VM tandem SC module used in the device optimized under the best optimization condition (Condition D in Fig. 11) are plotted in Fig. 12, with the load curve and η_{FE} of the EC reactor. Although η_{FE} is close to unity under the intense illumination of $P_{sun} = 90$ and 80 mW cm^{-2} (Conditions E and D, respectively), it lowers to 0.91 at $P_{sun} = 40$ mW cm^{-2} (Condition A). However, it should be noted that how much η_{FE} lowers depends on the EC reactor structure, catalysts used in the reactor, etc. It was confirmed again that the direct connection of the optimized VM SC module and EC module yields a higher $\eta_{CO}^{(annual)}$ than the use of a DC–DC converter; the numerical results are shown in Appendix B.

4.4. Application of wide E_g PVK SCs

In the previous subsections, the PVK SC with $E_g^{(PVK)} = 1.7$ eV was adopted for the design of the VM tandem SC modules because the performance of the PVK SCs with a wider $E_g^{(PVK)}$ than 1.7 eV is not sufficiently high at present.[15,16] Finally, we discuss the feasibility of improvements in $\eta_{SC}^{(annual)}$, $\eta_{H2}^{(annual)}$, and $\eta_{CO}^{(annual)}$ when highly efficient PVK SCs with a wider $E_g^{(PVK)}$ are realized. The fitting parameters of η_{EQE}, η_{ERE}, and r_s obtained in Sect. 3.1 were used, neglecting their $E_g^{(PVK)}$ dependences.

Figure 13(a) compares the $\eta_{SC}^{(annual)}$ values of the VM and 2T tandem SC modules as a function of $E_g^{(PVK)}$. The advantage of the VM module is the weak dependence on $E_g^{(PVK)}$, which is in contrast to the $\eta_{SC}^{(annual)}$ of the 2T module being strongly affected by $E_g^{(PVK)}$ because of the current matching problem.[28,29,31,32] Although $\eta_{SC}^{(annual)}$ of the VM module is maximized at $E_g^{(PVK)} = 1.84$ eV, the gain compared with the value at $E_g^{(PVK)} = 1.7$ eV is as small as 0.4%.

The results for the H_2- and CO-producing artificial photosynthetic devices using the VM-nEC configuration exhibit similar trends, as shown in Figs. 13(b) and 13(c), respectively. The maximal $\eta_{H2}^{(annual)}$ and $\eta_{CO}^{(annual)}$ at $E_g^{(PVK)} = 1.84$–1.85 eV are higher than those at $E_g^{(PVK)} = 1.7$ eV by only 0.3%–0.4%. Therefore, it is concluded that the room for improvements in $\eta_{SC}^{(annual)}$, $\eta_{H2}^{(annual)}$, and $\eta_{CO}^{(annual)}$ using a wider $E_g^{(PVK)}$ PVK SC is extremely narrow, and hence the focus should be further improvements in η_{SC} and durability with $E_g^{(PVK)} = 1.7$ eV.

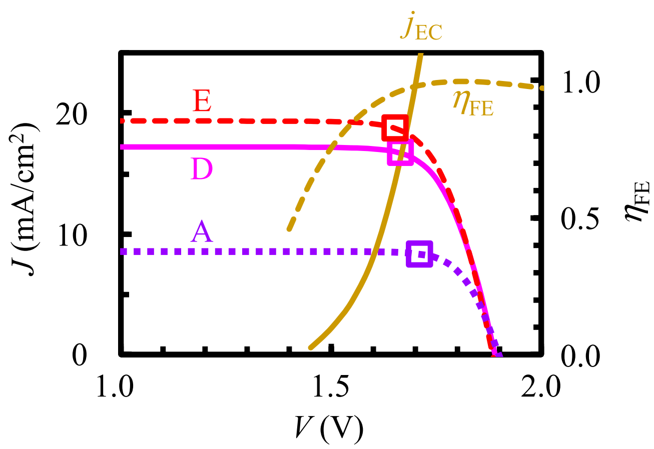

Fig. 12. J–V curves of the VM tandem SC module, and the load curve and η_{FE} of the EC module used in the VM-nEC CO-producing artificial photosynthetic device. The optimization condition is D used in Fig. 11, and the operating conditions are A, D, and E. The open square depicts V_{MPP} under each operating condition.

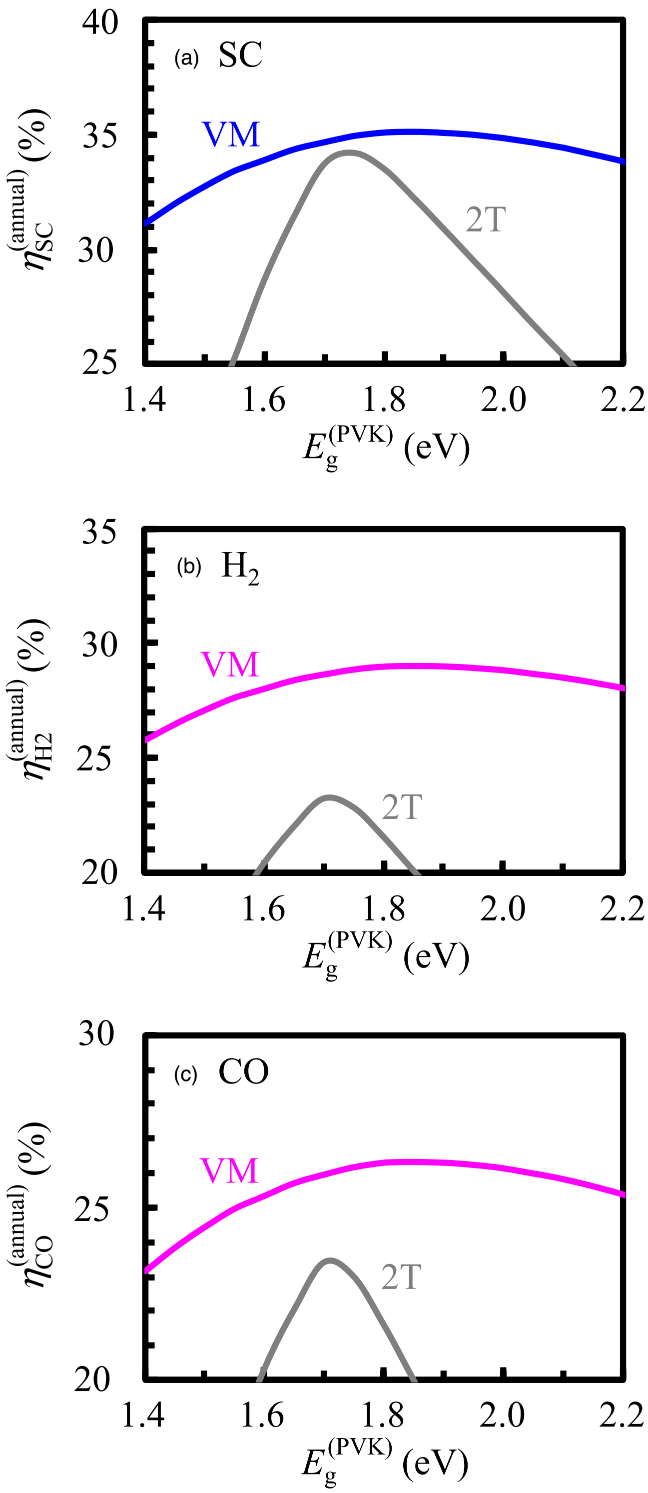

Fig. 13. (a) $\eta_{SC}^{(annual)}$ of the tandem SC modules, (b) $\eta_{H2}^{(annual)}$ of the H_2-producing artificial photosynthetic devices, and (c) $\eta_{CO}^{(annual)}$ of the CO-producing artificial photosynthetic devices dependent on $E_g^{(PVK)}$. The results for the VM modules and 2T modules are compared. The VM modules are optimized under the average condition for the SC modules in (a), whereas Condition D in Figs. 8 and 11 is adopted for the artificial photosynthetic devices in (b) and (c).

The maximal $\eta_{SC}^{(annual)}$ for the 2T SC module that satisfies the current matching under the optimization condition is close to that for the VM SC module.[28,29,31,32] By contrast, the maximal $\eta_{H2}^{(annual)}$ and $\eta_{CO}^{(annual)}$ for the 2T-EC devices are remarkably lower than those for the VM-*n*EC devices. This is because the optimal $E_g^{(PVK)}$ of the 2T modules are determined from the current matching condition, resulting in too high a V_{MPP} to power the present EC reactors.[28]

5. Conclusions

We have clarified the design guides for the H_2- and CO-producing artificial photosynthetic devices consisting of the VM PVK ($E_g^{(PVK)} = 1.7$ eV)/Si tandem SC modules and EC modules in which multiple EC reactors are connected in series. The design parameters of n_{PVK}/n_{EC} and n_{Si}/n_{EC} must be optimized under the conditions of slightly larger P_{sun} and higher T_{cell} than the average values, respectively. This is in contrast to that the VM tandem SC modules, whose configuration is characterized by n_{Si}/n_{PVK}, can be optimized under any practical conditions when they are coupled with power conditioners. Even if highly efficient PVK SCs with $E_g^{(PVK)} = 1.84–1.85$ eV are realized, $\eta_{H2}^{(annual)}$ and $\eta_{CO}^{(annual)}$ (and also $\eta_{SC}^{(annual)}$) improve by only 0.3%–0.5% relative to those at $E_g^{(PVK)} = 1.7$ eV.

Appendix A

When the VM tandem SC module operates under the optimization condition, the voltage matching holds, and hence η_{SC}

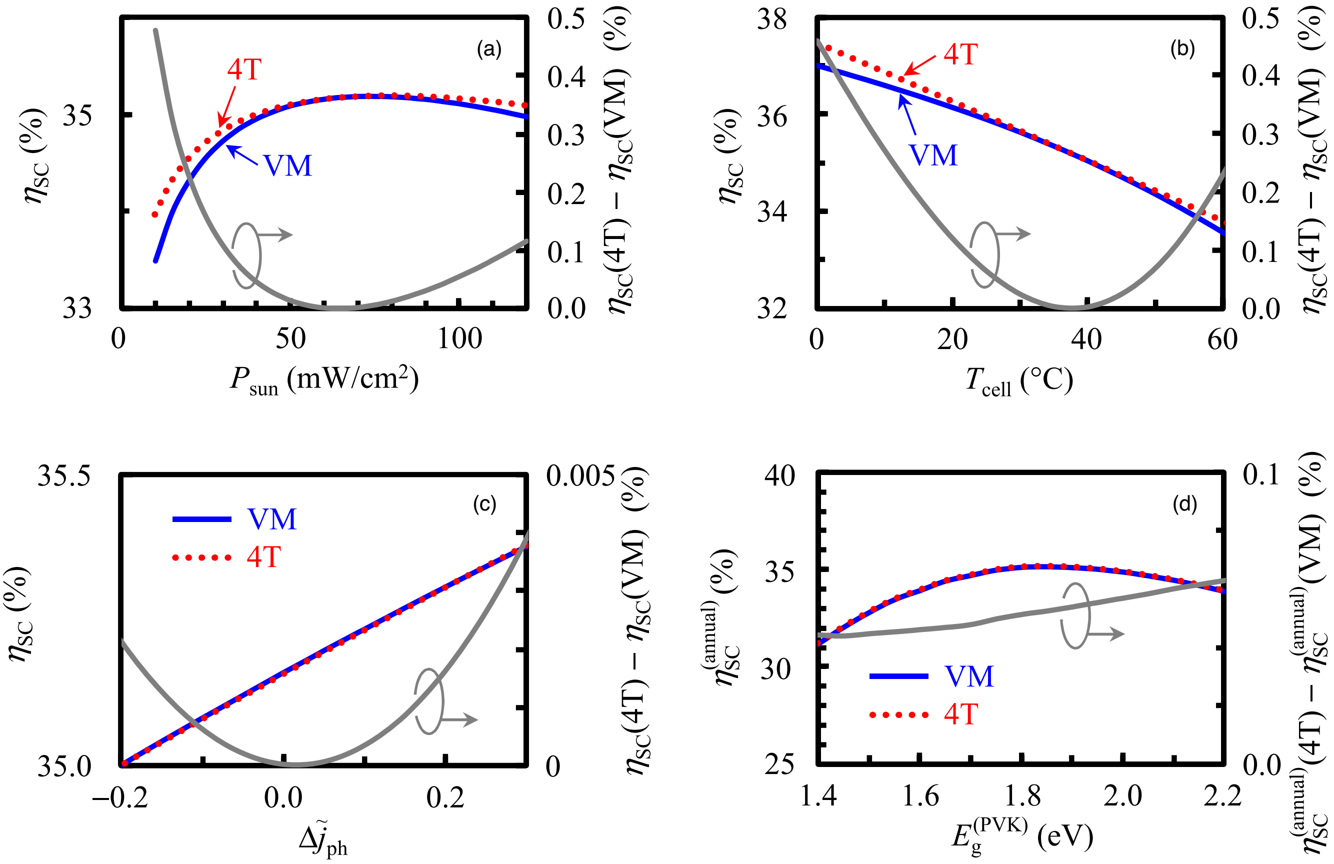

Fig. A·1. (a)–(c) Comparison of η_{SC} between the VM and 4T tandem SC modules. The optimization conditions for the VM module are the average conditions of $P_{sun} = \langle P_{sun} \rangle = 63.9$ mW cm^{-2}, $T_{cell} = \langle T_{cell} \rangle = 37.7$ °C, and $n_{sun}[\hbar\omega] = \langle n_{sun}[\hbar\omega] \rangle$ ($\Delta\tilde{j}_{ph} = 0.036$), resulting in $n_{Si}/n_{PVK} = 1.98$. The operating conditions are the average conditions except for the parameter of the horizontal axis in each figure. (d) $\eta_{SC}^{(annual)}$ of the VM and 4T modules dependent on $E_g^{(PVK)}$. In (c) and (d), the plots for the VM and 4T modules almost overlap with each other.

coincides with that of the 4T tandem SC module. However, η_{SC} lowers relative to the 4T value under different operating conditions, because the voltage matching breaks. Nevertheless, as shown in Figs. A·1(a)–A·1(c), the difference from η_{SC} of the 4T module is 0.2% at most, in the relevant range of the operating conditions: P_{sun} from 20 to 95 mW cm^{-2}, T_{cell} from 20 °C to 55 °C, and $\Delta\tilde{j}_{ph}$ from −0.05 to 0.2. Consequently, $\eta_{SC}^{(annual)}$ of the VM module, which is the average over various operating conditions, is virtually the same as that of the 4T module; the difference is as small as 0.05%, at $E_g^{(PVK)} = 1.7$–1.8 eV required for a high $\eta_{SC}^{(annual)}$[28,29,31,32]; see Fig. A·1(d).

Appendix B

In Sects. 4.2 and 4.3, it was found that the artificial photosynthetic devices consisting of the directly connected VM tandem SC modules and EC modules involve a voltage mismatching problem. Here, the two kinds of modules are connected via DC–DC converters (DDCs) to solve the problem. The VM modules should be optimized so that the output power (or η_{SC}) is maximized, like SC modules coupled with power conditioners. This offers an advantage that precise design is not required because $\eta_{SC}^{(annual)}$ is less sensitive to the optimization conditions than $\eta_{H2}^{(annual)}$ and $\eta_{CO}^{(annual)}$, as stated in Sect. 4.1.

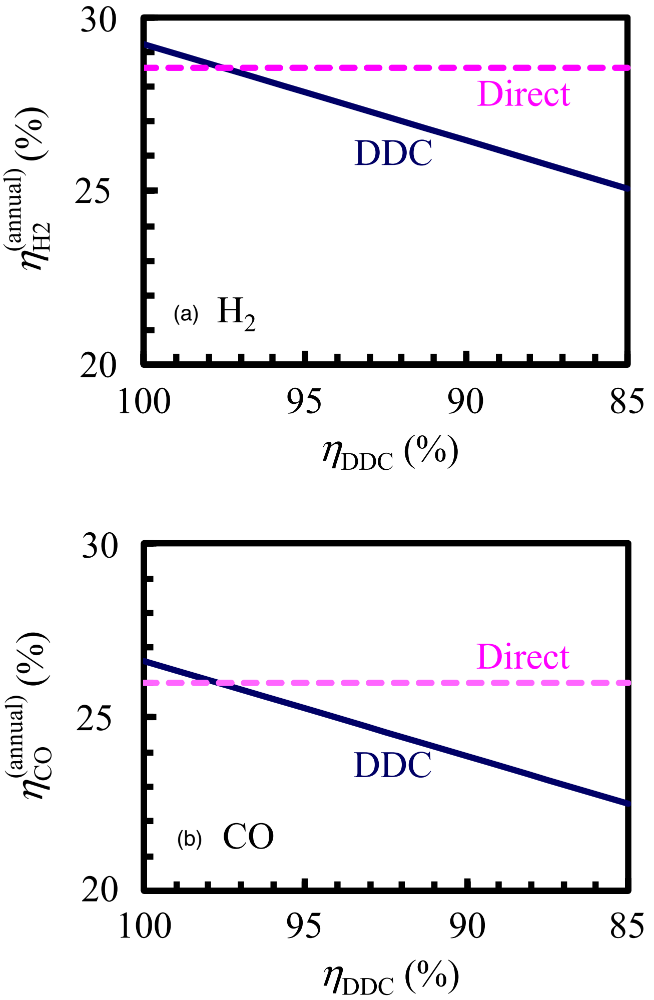

Fig. B·1. (a) $\eta_{H2}^{(annual)}$ and (b) $\eta_{CO}^{(annual)}$ of the artificial photosynthetic devices with two configurations: direct connection of the VM tandem SC modules and EC modules, and connection via DC–DC converters (DDCs). The VM modules used for the direct connection are optimized under Condition D in Figs. 8 and 11, whereas those used with DDCs under the average condition.

The operating point of the EC module changes depending on the DDC setting. The maximal value of J_{op} per a single EC reactor ($J_{op}^{(max)}$) and the corresponding voltage ($V_{op}^{(max)}$) are obtained by solving the following equation,

$$J_{op}^{(max)} = j_{EC}[V_{op}^{(max)}] = (J_{MPP} \cdot V_{MPP} \cdot \eta_{DDC})/V_{op}^{(max)}, \quad (15)$$

where η_{DDC} is the efficiency of the DC–DC conversion.

Figure B·1 shows the results of $\eta_{H2}^{(annual)}$ and $\eta_{CO}^{(annual)}$. Although η_{DDC} changes depending on the setting, it usually ranges from 90%–95%.[58,59] Thus, the direct connection of the VM tandem SC modules and EC modules yields higher η_{H2} and η_{CO} than the use of the DDCs.

ORCID iDs

Yasuhiko Takeda https://orcid.org/0000-0002-0874-4560
Ken-ichi Yamanaka https://orcid.org/0000-0002-0253-1740
Takeshi Morikawa https://orcid.org/0000-0002-4985-0925
Naohiko Kato https://orcid.org/0000-0001-9158-1549

1) M. Victoria et al., Joule **5**, 1041 (2021).
2) V. Romano, G. D'Angelo, S. Perathoner, and G. Centi, Energy Environ. Sci. **14**, 5760 (2021).
3) T. Morikawa, S. Sato, K. Sekizawa, T. M. Suzuki, and T. Arai, Acc. Chem. Res. **55**, 933 (2022).
4) W. Zhang, Z. Jin, and Z. Chen, Adv. Sci. **9**, 2105204 (2022).
5) N. Kato, S. Mizuno, M. Shiozawa, N. Nojiri, Y. Kawai, K. Fukumoto, T. Morikawa, and Y. Takeda, Joule **5**, 687 (2021).
6) N. Kato, Y. Takeda, Y. Kawai, N. Nojiri, M. Shiozawa, S. Mizuno, K. Yamanaka, T. Morikawa, and T. Hamaguchi, ACS Sustain. Chem. Eng. **9**, 16031 (2021).
7) M. Shiozawa, K. Kitazumi, M. Iwai, S. Mizuno, N. Kato, Y. Takeda, and T. Hamaguchi, Electrocatalysis **13**, 830 (2022).
8) Y. Takeda, S. Mizuno, R. Iwata, T. Morikawa, and N. Kato, J. CO2 Util. **71**, 102472 (2023).
9) F. Martinho, Energy Environ. Sci. **14**, 3840 (2021).
10) M. Yamaguchi, F. Dimroth, J. F. Geisz, and N. J. Ekins-Daukes, J. Appl. Phys. **129**, 240901 (2021).
11) S. P. Philipps, F. Dimroth, and A. W. Bett "High-efficiency III–V multijunction solar cells," *McEvoy's Handbook of Photovoltaics*, ed. S. A. Kalogirou (Academic, New York, 2018) 3rd ed., Chap. I-4-B.
12) A. R. bin, M. Yusoff, M. Vasilopoulou, D. G. Georgiadou, L. C. Palilis, A. Abate, and M. K. Nazeeruddin, Energy Environ. Sci. **14**, 2906 (2021).
13) Y. Cheng and L. Ding, Energy Environ. Sci. **14**, 3233 (2021).
14) G. Wu, R. Liang, M. Ge, G. Sun, Y. Zhang, and G. Xing, Adv. Mater. **34**, 2105635 (2022).
15) R. He et al., Energy Environ. Sci. **14**, 5723 (2021).
16) Y. Tong, A. Najar, L. Wang, L. Liu, M. Du, J. Yang, J. Li, K. Wang, and S. F. Liu, Adv. Sci. **9**, 2105085 (2022).
17) H. Min et al., Nature **598**, 444 (2021).
18) M. Kim et al., Science **375**, 302 (2022).
19) J. Liu et al., Science **377**, 302 (2022).
20) P. Tockhorn et al., Nat. Nanotechnol. **17**, 1214 (2022).
21) F. Fu, J. Li, T. C.-J. Yang, H. Liang, A. Faes, Q. Jeangros, C. Ballif, and Y. Hou, Adv. Mater. **34**, 2106540 (2022).
22) S. Pan et al., J. Mater. Chem. A **9**, 14085 (2021).
23) Y. Wang et al., Adv. Energy Mater. **11**, 2101053 (2021).
24) M. Wang, B. Shi, Q. Zhang, X. Li, S. Pan, Y. Zhao, and X. Zhang, Solar PRL **6**, 2100748 (2022).
25) J. Werner, F. Sahli, F. Fu, J. J. Diaz Leon, A. Walter, B. A. Kamino, B. Niesen, S. Nicolay, Q. Jeangros, and C. Ballif, ACS Energy Lett. **3**, 2052 (2018).
26) J. Zheng et al., ACS Energy Lett. **7**, 3003 (2022).
27) Y. Takeda, T. Morikawa, and N. Kato, J. Appl. Phys. **127**, 204503 (2020).
28) Y. Takeda, K. Yamanaka, T. Morikawa, and N. Kato, J. Appl. Phys. **132**, 075002 (2022).
29) M. H. Futscher and B. Ehrler, ACS Energy Lett. **1**, 863 (2016).

30) K. Alberi, J. Moore, K. Schmieder, M. Lumb, R. Walters, E. Armour, L. Mathew, and R. Rao, J. Photonics Energy **8**, 045504 (2018).
31) H. Liu, C. D. Rodríguez-Gallegos, Z. Liu, T. Buonassisi, T. Reindl, and I. M. Peters, Cell Rep. Phys. Sci. **1**, 100037 (2020).
32) J. Chantana, K. Takeguchi, Y. Kawano, and T. Minemoto, Renew. Energy **195**, 896 (2022).
33) T. M. Koh, H. Wang, Y. F. Ng, A. Bruno, S. Mhaisalkar, and N. Mathews, Adv. Mater. **34**, 2104661 (2022).
34) M. Nakamura, C. C. Lin, C. Nishiyama, K. Tada, T. Bessho, and H. Segawa, ACS Appl. Energy Mater. **5**, 8103 (2022).
35) W. Shockley and H. J. Queisser, J. Appl. Phys. **32**, 510 (1961).
36) U. Rau, Phys. Rev. B **76**, 085303 (2007).
37) P. Würfel, J. Phys. C: Solid State Phys. **15**, 3967 (1982).
38) M. A. Green and P. Photovolt, Res. Appl. **20**, 472 (2012).
39) Reference Solar Spectral Irradiance: Air Mass 1.5, National Renewable Energy Laboratory, available from: (https://rredc.nrel.gov/solar/spectra/am1.5/) (accessed October 1, 2022).
40) K. Yoshikawa et al., Nat. Energy **2**, 17032 (2017).
41) J. Nelson, *Physics of Solar Cells* (Imperial College Press, London, 2003).
42) S. Suckow, T. M. Pletzer, and H. Kurz, Prog. Photovolt.: Res. Appl. **22**, 494 (2014).
43) P. Hang, C. Kan, B. Li, Y. Yao, Z. Hu, Y. Zhang, J. Xie, Y. Wang, D. Yang, and X. Yu, Adv. Funct. Mater. **33**, 2214381 (2023).
44) B. Yu, F. Tang, Y. Yang, J. Huang, S. Wu, F. Lu, W. Duan, A. Lambertz, K. Ding, and Y. Mai, Adv. Mater. **35**, 2202447 (2023).
45) Y. Kato et al., Prog. Photovolt.: Res. Appl. **30**, 1198 (2022).
46) D. C. Nguyen, K. Sato, M. Hamada, F. Murata, and Y. Ishikawa, Sol. Energy **241**, 452 (2022).
47) E. Aydin, T. G. Allen, M. De Bastiani, L. Xu, J. Ávila, M. Salvador, E. Van Kerschaver, and S. De Wolf, Nat. Energy **5**, 851 (2020).
48) M. A. Green, Prog. Photovolt.: Res. Appl. **30**, 164 (2022).
49) M. Jošt, B. Lipovšek, B. Glažar, A. Al-Ashouri, K. Brecl, G. Matič, A. Magomedov, V. Getautis, M. Topič, and S. Albrecht, Adv. Energy Mater. **10**, 2000454 (2020).
50) J. Haschke et al., Energy Environ. Sci. **10**, 1196 (2017).
51) S. Wen, T. Yang, N. Zhao, L. Ma, and E. Liu, Appl. Catal. B **258**, 117953 (2019).
52) S. Verma, Y. Hamasaki, C. Kim, W. Huang, S. Lu, H.-R. M. Jhong, A. A. Gewirth, T. Fujigaya, N. Nakashima, and P. J. A. Kenis, ACS Energy Lett. **3**, 193 (2018).
53) Solar Radiation Database, New Energy and Industrial Technology Development Organization (NEDO).
54) B. Zhang, Q. Daniel, M. Cheng, L. Fan, and L. Sun, Faraday Discuss. **198**, 169 (2017).
55) L. Lin, H. Li, Y. Wang, H. Li, P. Wei, B. Nan, R. Si, G. Wang, and X. Bao, Angew. Chem. Int. Ed. **60**, 26582 (2021).
56) T. Du, W. Xu, S. Xu, S. R. Ratnasingham, C.-T. Lin, J. Kim, J. Briscoe, M. A. McLachlan, and J. R. Durrant, J. Mater. Chem. C **8**, 12648 (2020).
57) D. Glowienka and Y. Galagan, Adv. Mater. **34**, 2105920 (2022).
58) T. Sutikno, H. S. Purnama, N. S. Widodo, S. Padmanaban, and M. R. Sahid, Clean Energy **6**, 557 (2022).
59) O. M. Rodríguez-Benítez, J. A. Aqui-Tapia, I. Ortega-Velázquez, and G. Espinosa-Pérez, Electronics **11**, 2953 (2022).

